Respiratory Complexes III and IV Can each Bind Two Molecules of Cytochrome *c* at Low Ionic Strength

Blas Moreno-Beltrán[1], Irene Díaz-Moreno[1]*, Katiuska González-Arzola[1], Alejandra Guerra-Castellano[1], Adrián Velázquez-Campoy[2], Miguel A. De la Rosa[1] and Antonio Díaz-Quintana[1]

[1]Instituto de Bioquímica Vegetal y Fotosíntesis, cicCartuja, Universidad de Sevilla-CSIC, Avda. Américo Vespucio 49, Sevilla 41092, Spain

[2]Institute of Biocomputation and Physics of Complex Systems (BIFI) - Joint Unit BIFI-IQFR (CSIC), Universidad de Zaragoza, Mariano Esquillor s/n, 50018, Zaragoza, Spain; Departamento de Bioquímica y Biología Molecular y Celular, Universidad de Zaragoza, Pedro Cerbuna 12, 50009, Zaragoza, Spain; Fundacion ARAID, Government of Aragon, Maria de Luna 11, 50018, Spain

***Corresponding author:** idiazmoreno@us.es

Telephone number: +34 954489513; Fax number: +34 954460165

Abstract

The transient interactions of respiratory cytochrome *c* with complexes III and IV is herein investigated by using heterologous proteins, namely human cytochrome *c*, the soluble domain of plant cytochrome c_1 and bovine cytochrome *c* oxidase. The binding molecular mechanisms of the resulting cross-complexes have been analyzed by Nuclear Magnetic Resonance and Isothermal Titration Calorimetry. Our data reveal that the two cytochrome *c*-involving adducts possess a 2:1 stoichiometry – that is, two cytochrome *c* molecules per adduct – at low ionic strength. We conclude that such extra binding sites at the surfaces of complexes III and IV can facilitate the turnover and sliding of cytochrome *c* molecules and, therefore, the electron transfer within respiratory supercomplexes.

Keywords: Cytochrome *c*, Cytochrome bc_1, Cytochrome *c* oxidase, ITC, NMR, , Supercomplex.

Highlights:

- Plant cytochrome c_1, at its two binding sites, recognizes human cytochrome *c*.
- Docking of human cytochrome *c* at plant cytochrome c_1 is electrostatically driven.
- Cytochrome *c* oxidase can likewise house two molecules of cytochrome *c*.
- Extra binding sites for cytochrome *c* can facilitate its sliding in supercomplexes.

Abbreviations

Chemical-Shift Perturbations (CSP)

Cytochrome *bc*$_1$ (C*bc*$_1$)

Cytochrome *c* (C*c*)

Cytochrome *c* Oxidase (C*c*O)

Cytochrome *c*$_1$ (C*c*$_1$)

Complex III (III)

Complex IV (IV)

Dynamic Light Scattering (DLS)

Electron Transfer (ET)

Equilibrium dissociation constant (K_D)

Heteronuclear Single-Quantum Correlation (HSQC)

Human Cytochrome *c* (hC*c*)

Human Cytochrome *c*$_1$ (hC*c*$_1$)

Intermembrane Mitochondrial Space (IMS)

Inner Mitochondrial Membrane (IMM)

Isothermal Titration Calorimetry (ITC)

Luria-Bertani (LB)

Mitochondrial Matrix (MM)

Nuclear Magnetic Resonance (NMR)

Plant Cytochrome *c* (pC*c*)

Plant Cytochrome *c*$_1$ (pC*c*$_1$)

Principal Component Analysis (PCA)

Reduced Cytochrome *c* Oxidase (C*c*O$_{red}$)

Reduced human Cytochrome *c* (hC*c*$_{red}$)

Reduced plant Cytochrome *c*$_1$ (pC*c*$_{1red}$)

Introduction

Cytochrome c_1 (Cc_1) is the subunit of mitochondrial complex III (III), or Cytochrome bc_1 (Cbc_1), responsible for electron transfer (ET) to Cytochrome *c* (C*c*) and, in turn, to complex IV (IV), or Cytochrome *c* Oxidase (C*c*O) [1-5]. This function is essential for mitochondrial respiration, the major source of energy in eukaryotic cells. The organization of the mitochondrial electron transport chain is a subject of intense debate at present, where two different models are being considered: the fluid model, that proposes a random organization for individual respiratory protein components, and the solid model, suggesting a stable association between individual complexes [6-8]. Apart their role in respiration, C*c* and Cc_1 are clearly involved in the development of programmed cell death [9-15]. Such a dual role of C*c* is regulated by post-translational modifications – namely, phosphorylation and nitration of tyrosine residues – that affect the binding of C*c* to its physiological counterparts, either in the mitochondria or in the cytoplasm [16-23].

The ET reactions between C*c* and its partners Cbc_1 and C*c*O have been characterized by time-resolved spectroscopy and steady-state enzyme kinetic studies [24-28]. Both, reduction and oxidation of C*c* show multiphasic kinetic traces in polarographic and spectrophotometric studies. This suggests the presence of at least two binding sites in the C*c* partners: a catalytic ET site, along with an adjacent, non-productive site. In agreement with this, we have recently reported that plant C*c* (pC*c*) docks at two binding sites of plant Cc_1 (pCc_1) [29]: The first, *proximal* site is suitable for ET between both hemeproteins and resembles that previously determined by X-ray diffraction in yeasts [30]; the second, *distal* site localizes close to the Rieske subunit and seems to be involved in channeling of C*c* molecules towards C*c*O [29, 31, 32]. Classical crosslinking assays between C*c* and Cbc_1 had already pointed out that residues from the *distal* site of Cc_1 could be involved in the interaction with C*c* [33].

The study of heterologous complexes, also known as cross-complexes, is a widely accepted approach to get insight into the binding mode of interprotein complexes [34-35]. To provide further insight into the nature of the interactions between C*c* and Cc_1, we analyze here the cross-complex between human C*c* (hC*c*) and pCc_1, and compare it with the natural pC*c*-pCc_1 complex in plants in terms of binding affinity, specificity and dynamics. Actually, the turnover number for reduction of mammalian C*c* by potato Cbc_1 is similar than that for the mammalian C*c*-Cbc_1 system [28]. As there are substantial differences in the electrostatic potential surface of pC*c* and hC*c*, the analysis of the hC*c*-pCc_1 complex is a very useful approach to better understand the C*c*-Cc_1 binding mode. In fact, the major differences between the two C*c* orthologs are at their respective surfaces in contact with pCc_1 (Figure 1). Given the relevance of electrostatics in C*c*-Cc_1 complexes, the ionic-strength dependence of the binding event has also been addressed, so revealing a crucial role in both the binding affinity between the partners and the definition of the binding sites on the pCc_1 surface. In addition, the hC*c*-pCc_1 interaction has been compared with that between hC*c* and bovine C*c*O. Notably, C*c* also interacts with two binding sites on C*c*O. Altogether, our data provide a better comprehension of the molecular recognition processes involved in mitochondrial respiration.

Material and Methods

Modelling

pC*c* and pCc_1 models were built in previous work [29]. hC*c* structure was taken from Protein Data Bank (PDB ID: 3zcf) [36]. Human cytochrome c_1 (hCc_1) model was built following the same procedure reported for pCc_1 model [29]. The electrostatic potential surfaces of pC*c*, pCc_1, hC*c*, and hCc_1 structures were calculated using DelPhi [37] and Chimera [38]. The electrostatic potential surfaces were calculated assuming an ionic strength of 250 mM.

Protein Expression and Purification

Escherichia coli BL21 (DE3) cells transformed with pBTR1 plasmid were used to produce recombinant hC*c* [39]. ^{15}N-labeled hC*c* was expressed in M9 minimal medium for Nuclear Magnetic Resonance (NMR) titrations, whereas unlabeled hC*c* was produced in Luria-Bertani (LB) medium for Isothermal Titration Calorimetry (ITC) measurements. Expression and purification protocol was similar to that recently described for pC*c* [29], excepting the cell culture was at 30 ºC and the elution gradient for the cationic exchange column, which ranged from 0.036 to 0.36 M NaCl. The optimization of the expression and purification steps was carried out according to specific protocols for *c*-type cytochromes [40-43]. The yield of hC*c* was 15-20 mg / L in LB and 10-15 mg / L in M9 minimal medium.

Unlabeled pCc_1 was expressed and purified as described previously [29].

Bovine C*c*O was purchased from Sigma and used after exchanging its buffer in Millipore 3K NMWL centricons to 10 mM sodium phosphate buffer (pH 7.4) containing 0.2% n-Dodecyl-β-D-maltoside and 5 mM sodium dithionite. The pH of the buffer was checked before and after the sample preparation. Fresh samples were used to carry out the experiments. Dynamic Light Scattering (DLS) assays were performed to

evaluate the oligomerization state of the C*c*O at the protein concentration used in ITC titrations, in which C*c*O was predominantly monomeric (75%). DLS experiments were conducted at 25 ºC in a Zetasizer Nano ZS (Malvern).

NMR measurements

NMR assignments of the ^{15}N and ^{1}H nuclei of reduced hC*c* (hCc_{red}, BMRB accession number 5406) were taken from a previous work [44].

NMR titrations of 100 μM of ^{15}N labeled hCc_{red} with aliquots of unlabeled reduced pCc_1 (pCc_{1red}) were performed at 25 ºC and recorded on a Bruker Avance 700 MHz. Titrations were performed in 5 mM sodium phosphate pH 6.3 with 10% D_2O, in the presence and in the absence of 50 mM NaCl. Each titration step was prepared in an independent NMR tube (Shigemi) up to a 0.28 mL volume. The Chemical-Shift Perturbations (CSP) were monitored in a series of [^{1}H, ^{15}N] Heteronuclear Single-Quantum Correlation (HSQC) experiments. The data were processed using Bruker TOPSPIN and analyzed with SPARKY (Goddard and Kneller, SPARKY 3, University of California, San Francisco). CSP titration curves were analyzed using one-site and two-site binding models, as previously described [29].

Additionally, ^{15}N-labeled hCc_{red} and unlabeled pCc_{1red} at a ratio of 1:2, was titrated with increasing concentrations of NaCl. Each titration step was prepared in the same tube and the pH of the samples was also checked for each spectrum. The chemical-shift changes were monitored, processed and analyzed as described before. Data were also analyzed by Principal Component Analysis (PCA) according to previous work [29].

ITC Measurements

All ITC experiments were performed using an Auto-ITC200 instrument (MicroCal, GE Healthcare) at 25 ºC. The reference cell was filled with distilled water. The titration experiments between hCc_{red} and pCc_{1red} consisted in 2 μL injections of 0.4 mM hCc_{red}

in 10 mM sodium phosphate buffer pH 7.4 in the absence and in the presence of additional 50 and 100 mM NaCl into the sample cell, initially containing a 20 μM pCc_{1red} solution in the same buffer. A titration was also carried out with the oxidized forms of hC*c* and pCc_1 in 10 mM sodium phosphate buffer pH 7.4 in the absence of additional NaCl. Besides, a titration of reduced C*c*O (C*c*O$_{red}$, 3.85 μM) with hCc_{red} (0.10 mM) was performed in 10 mM sodium phosphate pH 7.4 containing 0.2% n-Dodecyl-β-maltoside and 5 mM sodium dithionite. All solutions were degassed before titrations. Titrant was injected at appropriate time intervals to ensure that the thermal power signal returned to the baseline prior to the next injection. To achieve homogeneous mixing in the cell, the stirring speed was kept constant at 1,000 rpm. The data, specifically the heat per injection normalized per mol of injectant *versus* molar ratio, were analyzed with Origin 7 (OriginLab) using one-site and two-site binding models [45]. Calibration and performance tests of the calorimeter were carried out conducting Ca^{+2}-EDTA titrations with solutions provided by the manufacturer.

Results and Discussion

The heterologous hC*c*-pCc_1 complex

The cross complex was first studied by NMR. [^{1}H, ^{15}N] HSQC spectra were recorded along a titration of ^{15}N-labeled hC*c* with unlabeled pCc_1. Several amide signals exhibited significant CSP (Figure 2a,b). The perturbation pattern was consistent with a fast/intermediate exchange rate on the NMR time scale. The CSP data in Figure 2b,c show that few residues have $\Delta\delta_{avg}$ larger than 0.075 ppm, namely Gln16, Ala50, Ala51, Lys72, Gly77, Ile81 and Lys86. These residues are surrounding the heme crevice and constitute the interaction surface (Figure 2c), which is very well-conserved among complexes involving *c*-type cytochromes [14, 29, 46-55]. In addition, significant CSP are detected ($\Delta\delta_{avg} \geq 0.05$ ppm) for Lys7, Lys13, Val20, Ser47, Lys73, Val83, Lys88 and Ala92. Interestingly, Lys8, Lys13, Lys27, Lys72, Lys86 and Lys87 are all in contact with pCc_1, as previously reported in chemical modification studies and molecular dynamics simulations [56-58].

When compared with pC*c* upon binding to pCc_1 [29], the map of CSP on the hC*c* surface differs at the level of those residues located far from the heme cleft. In particular, the hydrophobic patch containing Ile11 was not affected in hC*c*, whereas two basic regions of hC*c* were substantially perturbed (Figure 2c). These regions comprise many charged residues, such as Lys25, Lys27, Lys86, Lys88 and Arg91. The observed differences in the binding surface, of the two C*c* molecules correlated well with the differences in the electrostatic potential maps and the sequence alignments of both C*c* species shown in Figure 1 and Figure S1. Notably, several amino acid changes (Lys39 by Gln, Pro167 by Lys and Thr171 by Asp) modify the charge configuration at the *proximal* binding site of hCc_1 with respect to that of pCc_1. Still, these differences seem not to affect the affinity between the partners (see below). This suggests a higher contribution of the electrostatic forces in the cross complex, which can modulate the

specificity and dynamics of the interaction. On the other hand, the differences in the electrostatic potential surfaces and sequences of hC*c* and pC*c* might be correlated with the sequence differences found at the *proximal* site of hCc_1 and pCc_1 (Figure S1), insofar as the ET may be optimum within the physiological complexes [59, 60]. In addition, Lys27, which is involved in the binding of hC*c* to Apaf-1 to trigger programed cell death [39], was affected in the cross-complex but not in the pC*c*-pCc_1 complex (Lys35 in pC*c*).

The CSP binding curves consistently fitted to a 2:1 binding model assuming two independent sites on pCc_1 with distinct affinities (Figure 2d and Figure S2a). The R^2 and χ^2 values were 0.9931 and 1.1×10^{-4}, respectively. Remarkably, the binding curves of CSP hardly fitted to a 1:1 binding model, as shown for the –NH group of Gln16 (Figure 2e). In this case, the R^2 and χ^2 values were 0.7872 and 0.1076, respectively. Therefore, our data clearly suggest the presence on the pCc_1 surface of two independent binding sites for hC*c*, as does for pC*c*. The equilibrium dissociation constants (K_D) were 0.30 μM and 40 μM for the *proximal* and *distal* binding sites, respectively (Table 1), similar to those previously reported for the physiological plant pC*c*-pCc_1 complex [29]. However, when the two sites were forced to show a similar K_D, the resulting fit was not so good, with R^2 and χ^2 values of 0.9782 and 5.5×10^{-3}, respectively.

In order to obtain accurate data on the binding affinities for oxidized complexes, ITC experiments were performed (Figure 3). The experimental data for both redox states fit to a 2:1 model with distinct K_D values. Reduced χ^2 values were 464 and 286 for the reduced and oxidized proteins, respectively. As shown in Figure 3 and Table 1, data are consistent with a first site for tight binding and another site for a weaker, more transient interaction, in agreement with a previous report [29]. Notably, the redox state of the hemeproteins hardly affected the observed affinities. The differences in K_D values obtained by ITC and NMR can be explained by the distinct physical phenomena

measured. The binding reaction was endothermic and entropically driven in both reduced and oxidized complexes, being the enthalpic contribution to the binding quite unfavorable (11.7 and 6.2 kcal mol^{-1}, respectively). Once again, the fit was slightly worse when forced to a single K_D value for the two sites (reduced χ^2 values were 2,453 and 447). In that case, K_D values were 9.1 μM and 13.0 μM for the reduced and oxidized complexes, respectively.

Ionic strength dependence on the hC*c*-pCc_1 interaction

Given the relevance of electrostatic forces in transient interactions [61-64] and, in particular, in the C*c*-Cc_1 complex [1, 5, 56-58], we analyzed the ionic strength dependence of the binding mode of hC*c* on pCc_1. [^{1}H, ^{15}N] HSQC spectra were recorded on a hC*c*:pCc_1 (2:1) sample, over a range of NaCl concentrations (0 - 320 mM). At 80 mM NaCl, the magnitude of the $\Delta\delta_{bind}$ values decreased by 60% on average, as shown for both dimensions (Figure 2f and Figure S2b), which indicated a strong electrostatic contribution to the complex formation. PCA of such titration showed that the three main components explained 95.7% of the changes (Figure S3). The first component accounted for a 68.6% and its projection decreased monotonically with ionic strength. The second one accounted for a 20.8% and showed a minimum value at 45 mM ionic strength. The third one accounted for a 6.3% and showed a more complex pattern, but still displaying a minimum at 45 mM.

Additional NMR and ITC titrations at different NaCl concentrations were performed in order to understand how the stoichiometry and the binding affinity of the interaction between hC*c* and pCc_1 were modulated by ionic strength. First, a direct NMR titration was carried out in the presence of additional 50 mM NaCl. [^{1}H, ^{15}N] HSQC spectra were recorded along a titration of ^{15}N-labeled hC*c* with unlabeled pCc_1. Only a few amide signals exhibited CSP, whose magnitudes were smaller than those calculated at

low ionic strength (Figure 2d, Figure S4). Notably, binding curves of CSP for these amide groups could be reliably fitted to a 1:1 model with a single K_D of *ca.* 12.8 μM (Figure S4). The R^2 and χ^2 values were 0.9821 and 0.01314, respectively. According to statistical criteria, the fit did not improve significantly when using a 2:1 binding model. In that case, the R^2 and χ^2 values were 0.9828 and 0.01077.

ITC titrations were further performed in the presence of additional 50 and 100 mM NaCl. In both cases, binding could only be accurately fitted to a 1:1 model, with a K_D value equal to 69 and 230 μM, respectively (Table 1, Figure S5). The affinity is smaller than that obtained for both the *proximal* and *distal* sites at low ionic strength (11 and 54 μM, respectively). There was also an increase in the enthalpic contribution at 100 mM NaCl in comparison with the titration performed at low ionic strength. This finding can be attributed to the lower electrostatic attraction between the two partners at higher ionic strength.

The salt titrations thus revealed that a single binding site for hC*c* on the pCc_1 surface remains populated enough to be detected by CSP at high ionic strength. Actually, the crystal structure of the yeast C*c*-C*bc*$_1$ complex shows a single binding site for C*c*, as it was solved at an ionic strength of *ca*. 120 mM [30]. Given the negative charge of the *distal* site of pCc_1 and its weak affinity for C*c* at low ionic strength [29], we can assume that it is the *proximal* site which remains at high ionic strength although its binding affinity decreases along NaCl titration. On the other hand, the *distal* site may remain as a local minimum of the interaction path, forming part of the encounter ensemble or showing a highly dynamic behavior. Like in analogous ET complexes in photosynthesis, CSP may be insensitive enough to describe the whole ensemble [54, 65], so further work will be required to display these features.

Interaction between hC*c* and bovine C*c*O

Kinetic-based models have proposed the existence of alternative, non-productive binding sites for horse C*c* in bovine C*c*O [26, 27]. Recently, the surface residues of hC*c* contacting bovine C*c*O have been mapped by NMR [52]. However, no evidences on the stoichiometry and binding affinity of the C*c*-C*c*O complex were elucidated by NMR. Direct binding studies performed by gel filtration between several mammalian C*c* and bovine C*c*O evidenced a 2:1 stoichiometry, in which C*c* binds to a first site with a dissociation constant in the nanomolar range and to a second site with less affinity [66]. Hence, we performed ITC titration experiments to compare its binding mode with that of the hC*c*-pCc_1 interaction and to confirm the stoichiometry of the hC*c*-C*c*O complex in equilibrium conditions.

Our experimental data using hC*c* and bovine C*c*O accurately fit to a model of two independent binding sites with distinct affinity values for hC*c* on C*c*O at low ionic strength, being the K_{D1} equal to 30 nM and the K_{D2} equal to 0.30 μM (Figure 4). χ^2 value was 84,825. The monomeric state of bovine C*c*O was predominant at the concentration used for this titration, as was estimated by DLS assays (Figure S6). Notably, binding isotherms could not be accurately fitted to a 1:1 binding model. Nevertheless, binding isotherms could be fitted to a model of 2 independent sites with an identical K_D value of 0.27 μM for the two binding sites. In this case, χ^2 value was 92,208, suggesting that this fit is slightly worse than the previous 2:1 binding model with distinct K_D values. This result is consistent with direct binding studies performed by gel filtration [66]. The binding affinity for this complex was one-two orders of magnitude tighter than those calculated for the hC*c* on the *proximal* site of pCc_1, according to the K_D values provided by ITC. These differences could be ascribed to the use of the entire membrane-bound C*c*O in contrast with pCc_1, as well as to the distinct organisms employed, as previously suggested for cyanobacterial respiratory complexes [67]. In addition, the hC*c*-C*c*O binding reaction was exothermic. The value for the enthalpic contribution (ΔH) was - 6.8 kcal mol^{-1} for the 2:1 binding model with an identical K_D

value, whereas ΔH_1 and ΔH_2 were - 6.6 and - 5.4 kcal mol^{-1}, respectively, when the 2:1 binding model with distinct K_D values was used. In addition, the reaction was favored by both enthalpic and entropic contributions, thereby suggesting that both polar and non-polar interactions control the complex formation, as previously suggested [52]. The entropic contribution (-TΔS) was - 2.1 kcal mol^{-1} for the 2:1 binding model with an identical K_D value, whereas -TΔS_1 and -TΔS_2 were - 3.6 and - 3.4 kcal mol^{-1}, respectively, when the 2:1 binding model with distinct K_D values was used.

The presence of additional binding sites for C*c* in both pC*c*$_1$ and C*c*O could open new perspectives on the mitochondrial electron transport chain, where membrane respiratory complexes can be either in independent, free diffusional motion or forming macromolecular assemblies, the so-called supercomplexes [3]. In this context, such new binding sites for C*c* on the surface of its physiological counterparts, C*bc*$_1$ and C*c*O, could facilitate the turnover and sliding mechanisms of C*c* molecules in plant and mammalian supercomplexes (Figure 5) [29, 32, 55]. Indeed, the accommodation of several C*c* molecules between C*bc*$_1$ and C*c*O in supercomplexes could provide a path for C*c* diffusion from C*bc*$_1$ to C*c*O. That diffusion path might have physiological significance in the electron flow, which is controlled in supercomplexes to optimize the use of available substrates [68]. The existence of extra binding sites could also be useful just to attract C*c* molecules near its ET binding domains.

Acknowledgments

We thank Dr. Manuel Angulo and Dr. Encarnación Zafra for assistance in the NMR data collection at CITIUS NMR Facility of the University of Seville. Financial support was provided by the Spanish Ministry of Economy and Competitiveness (Grant Nos. BFU2010-19451/BMC and BFU2012-31670/BMC) and by the Andalusian Government (Grant PAI, BIO198). BMB was awarded with a PhD fellowship (AP2009-4092) from the Spanish Ministry of Education, co-funded by European Social Fund-ERDF (2007–2013). AGC was awarded with a PhD fellowship from CSIC (JaePre-2011-01248), co-funded by European Social Fund-ERDF (2007-2013). All authors declare no conflict of interest.

Figure Legends

Figure 1. Electrostatic surface potential of hC*c* and pC*c*.

Negatively and positively charged regions of hC*c* (*upper*) and pC*c* (*lower*) surfaces are depicted in red and blue colors, respectively. The color scale ranges from -5 (red) to +5 (blue) k_BT. Some residue numbers have been mapped to better show the orientation of hC*c* and pC*c* in the figure. The arrows highlight two electropositive regions at the hC*c* surface. The simulation was performed using DelPhi aided by Chimera, assuming an ionic strength of 250 mM. The interior and exterior dielectric constants were fixed to 2 and 80, respectively.

Figure 2. NMR binding experiments with reduced hC*c*-pCc_1 complex.

a) Detail of the superimposed [^{1}H, ^{15}N] HSQC spectra of ^{15}N-labeled hC*c* along titration with pCc_1. hC*c* concentration was 100 μM at each titration step. Signals corresponding to distinct titration steps are colored according to the code in the panel. **b)** Plot of CSP of ^{15}N-labeled hC*c* as a function of residue number. Proline and non-assigned residues are marked by asterisks. The color bars point out the $\Delta\delta_{avg}$ categories, as follows: insignificant <0.025 ppm (blue), small 0.025-0.050 ppm (yellow), medium 0.050-0.075 ppm (orange) and large >0.075 ppm (red). **c)** CSP map of reduced hC*c* upon addition of reduced pCc_1. Residues are colored according to the $\Delta\delta_{avg}$ categories, as indicated in b). **d)** Curves representing the best global fit of several amide signals in the direct dimension for an hC*c*:pCc_1 binding model with two different global K_D values. **e)** Binding curves of the Gln16 residue in the direct dimension. Lines represent the best fit to 1:1 (red) or 2:1 (black) binding models. **f)** Salt dependence of the $|\Delta\delta_{bind}|$ values in the direct dimension for all backbone amide resonances observed in the hC*c*-pCc_1 complex.

Figure 3. ITC binding experiments corresponding to the reduced and oxidized hC*c*-pCc_1 complexes.

Binding assays corresponding to the complexes between hC*c* and pCc_1 were performed under reducing (*left*) or oxidizing conditions (*right*). Experimental data for both redox states were fitted to a two-site binding model. Thermograms and isotherms are shown at the *upper* and *lower* panels, respectively.

Figure 4. ITC binding experiment corresponding to the reduced hC*c*-C*c*O complex.

Binding assay corresponding to the complex between hC*c* and bovine C*c*O was performed under reducing conditions. Experimental data were fitted to a two-site binding model. The thermogram is shown at the *upper* panel and the binding isotherm at the *lower* panel.

Figure 5. Two different models for the role played by C*c* in transferring electrons between complexes III and IV.

Diagrams of the respiratory mitochondrial chain including two different scenarios, the formation of the supercomplex composed by dimeric C*bc*$_1$ and C*c*O complexes (*left*) or free C*bc*$_1$ and C*c*O complexes in diffusional motion (*right*). Complexes are viewed parallel to the plane of the inner mitochondrial membrane (IMM) with the intermembrane space (IMS) oriented to the top (*upper*), as well as perpendicular to the plane of the IMM (*down*). C*c* is represented as red balls at its binding sites on C*bc*$_1$ (tan) and C*c*O (green). Two binding sites are represented in each complex. Channeling of C*c* molecules between C*bc*$_1$ and C*c*O is marked by arrows in the supercomplex rearrangement. Mitochondrial matrix (MM) is also indicated in the upper diagram.

Supplementary Material:

Supplementary material associated with this article can be found in the online version.

References

1. M. Sarewicz, A. Borek, F. Daldal, W. Froncisz, A. Osyczka, Demonstration of short-lived complexes of cytochrome *c* with cytochrome bc_1 by EPR spectroscopy: implications for the mechanism of interprotein electron transfer, *J. Biol. Chem.* 283 (2008) 24826-24836.
2. L. Geren, B. Durham, F. Millett, Use of ruthenium photoreduction techniques to study electron transfer in cytochrome oxidase, *Methods Enzymol.*, 456 (2009) 507-520.
3. G. Lenaz, M.L. Genova, Structure and organization of mitochondrial respiratory complexes: a new understanding of an old subject, *Antioxid. Redox Signal*. 12 (2010) 961-1008.
4. I. Díaz-Moreno, J.M. García-Heredia, A. Díaz-Quintana, M.A. De la Rosa, Cytochrome *c* signalosome in mitochondria, *Eur. Biophys. J.* 40 (2011) 1301-1315.
5. F. Millett, J. Havens, S. Rajagukguk, B. Durham, Design and use of photoactive ruthenium complexes to study electron transfer within cytochrome bc_1 and from cytochrome bc_1 to cytochrome *c*, *Biochim. Biophys. Acta* 1827 (2013) 1309-1319.
6. C.R. Hackenbrock, B. Chazotte, S.S. Gupte, The random collision model and a critical assessment of diffusion and collision in mitochondrial electron transport, *J. Bioenerg. Biomembr.* 18 (1986) 331-368.
7. R. Acín-Pérez, P. Fernández-Silva, M.L. Peleato, A. Pérez-Martos, J.A. Enríquez, Respiratory active mitochondrial supercomplexes, *Mol. Cell*. 32 (2008) 529-539.
8. M. Trouillard, B. Meunier, F. Rappaport, Questioning the functional relevance of mitochondrial supercomplexes by time-resolved analysis of the respiratory chain, *Proc. Natl. Acad. Sci. U. S. A.* 108 (2011) 1027-1034.

9. H. Zou, Y. Li, X. Liu, X. Wang, An APAF-1-cytochrome *c* multimeric complex is a functional apoptosome that activates procaspase-9, *J. Biol. Chem*. 274 (1999) 11549-11556.
10. J.M. García-Heredia, M. Hervás, M.A. De la Rosa, J.A. Navarro, Acetylsalicylic acid induces programmed cell death in *Arabidopsis* cell cultures, *Planta* 228 (2008) 89-97.
11. C.E. Bender, P. Fitzgerald, S.W. Tait, F. Llambi, G.P. McStay, D.O. Tupper, J. Pellettieri, A. Sánchez-Alvarado, G.S. Salvesen, D.R. Green, Mitochondrial pathway of apoptosis is ancestral in metazoans, *Proc. Natl. Acad. Sci.* USA 109 (2012) 4904-4909.
12. Y. Zhu, M. Li, X. Wang, H. Jin, S. Liu, J. Xu, Q. Chen, Caspase cleavage of cytochrome c_1 disrupts mitochondrial function and enhances cytochrome *c* release, *Cell Res.* 22 (2012) 127-141.
13. J. Martínez-Fábregas, I. Díaz-Moreno, K. González-Arzola, S. Janocha, J.A. Navarro, M. Hervás, R. Bernhardt, A. Díaz-Quintana, M.A. De la Rosa, New *Arabidopsis thaliana* cytochrome *c* partners: A look into the elusive role of cytochrome *c* in programmed cell death in plants, *Mol. Cell. Proteomics* 12 (2013) 3666-3676.
14. J. Martínez-Fábregas, I. Díaz-Moreno, K. González-Arzola, S. Janocha, J.A. Navarro, M. Hervás, R. Bernhardt, A. Velazquez-Campoy, A. Díaz-Quintana, M.A. De la Rosa, Structural and functional analysis of novel human cytochrome *c* targets in apoptosis, *Mol. Cell. Proteomics* 13 (2014a) 1439-1456.
15. J. Martínez-Fábregas, I. Díaz-Moreno, K. González-Arzola, A. Díaz-Quintana, M.A. De la Rosa, A common signalosome for programmed cell death in humans and plants, *Cell. Death. Dis.* 5 (2014b) e1314.
16. V. Rodríguez-Roldán, J.M. García-Heredia, J.A. Navarro, M.A. De la Rosa, M. Hervás, Effect of nitration on the physicochemical and kinetic features of wild-

type and monotyrosine mutants of human respiratory cytochrome *c*, *Biochemistry* 47 (2008) 12371-12379.

17. H. Yu, I. Lee, A.R. Salomon, K. Yu, M. Hüttemann, Mammalian liver cytochrome *c* is tyrosine-48 phosphorylated in vivo, inhibiting mitochondrial respiration, *Biochim. Biophys. Acta* 1777 (2008) 1066-1071.
18. L.A. Abriata, A. Cassina, V. Tórtora, M. Marín, J.M. Souza, L. Castro, A.J. Vila, R. Radi, Nitration of solvent-exposed tyrosine 74 on cytochrome *c* triggers heme iron-methionine 80 bond disruption. Nuclear magnetic resonance and optical spectroscopy studies, *J. Biol. Chem.* 284 (2009) 17-26.
19. J.M. García-Heredia, I. Díaz-Moreno, P.M. Nieto, M. Orzáez, S. Kocanis, M. Teixeira, E. Pérez-Payá, A. Díaz-Quintana, M.A. De la Rosa, Nitration of tyrosine 74 prevents human cytochrome *c* to play a key role in apoptosis signaling by blocking caspase-9 activation, *Biochim. Biophys. Acta* 1797 (2010) 981-993.
20. J.M. García-Heredia, A. Díaz-Quintana, M. Salzano, M. Orzáez, E. Pérez-Payá, M. Teixeira, M.A. De la Rosa, I. Díaz-Moreno, Tyrosine phosphorylation turns alkaline transition into a biologically relevant process and makes human cytochrome *c* behave as an anti-apoptotic switch, *J. Biol. Inorg. Chem.* 16 (2011) 1155-1168.
21. I. Díaz-Moreno, J.M. García-Heredia, A. Díaz-Quintana, M. Teixeira, M.A. De la Rosa, Nitration of tyrosines 46 and 48 induces the specific degradation of cytochrome *c* upon change of the heme iron state to high-spin, *Biochim. Biophys. Acta* 1807 (2011) 1616-1623.
22. J.M. García-Heredia, I. Díaz-Moreno, A. Díaz-Quintana, M. Orzáez, J.A. Navarro, M. Hervás, M.A. De la Rosa, Specific nitration of tyrosines 46 and 48 makes cytochrome *c* assemble a non-functional apoptosome, *FEBS Lett*. 586 (2012) 154-158.

23. H.K. Ly, T. Utesch, I. Díaz-Moreno, J.M. García-Heredia, M.A. De la Rosa, P. Hildebrandt, Perturbation of the redox site structure of cytochrome *c* variants upon tyrosine nitration, *J. Phys. Chem. B.* 116 (2012) 5694-5702.

24. C.A. Yu, L. Yu, T.E. King, Kinetics of electron transfer between cardiac cytochrome c_1 and *c*. *J. Biol. Chem.* 248 (1973) 528-533.

25. S.H. Speck, E. Margoliash, Characterization of the interaction of cytochrome *c* and mitochondrial ubiquinol-cytochrome *c* reductase, *J. Biol. Chem*. 259 (1984) 1064-1072.

26. S.H. Speck, D. Dye, E. Margoliash, Single catalytic site model for the oxidation of ferrocytochrome *c* by mitochondrial cytochrome *c* oxidase, *Proc. Natl. Acad. Sci.* USA 81 (1984) 347-351.

27. E.A. Garber, E. Margoliash, Interaction of cytochrome *c* with cytochrome *c* oxidase: an understanding of the high- to low-affinity transition, *Biochim. Biophys. Acta* 1015 (1990) 279-287.

28. E. A. Berry, L. Huang, V.J. DeRose, Ubiquinol-cytochrome *c* oxidoreductase of higher plants, *J. Biol. Chem.* 266 (1991) 9064-9077.

29. B. Moreno-Beltrán, A. Díaz-Quintana, K. González-Arzola, A. Velázquez-Campoy, M.A. De la Rosa, I. Díaz-Moreno, Cytochrome c_1 exhibits two binding sites for cytochrome *c* in plants, *Biochim. Biophys. Acta* 1837 (2014) 1717-1729.

30. C. Lange, C. Hunte, Crystal structure of the yeast cytochrome bc_1 complex with its bound substrate cytochrome *c*, *Proc. Natl. Acad. Sci.* USA 99 (2002) 2800-2805.

31. B.N. Kholodenko, H.V. Westerhoff, Metabolic channelling and control of the flux, *FEBS Lett*. 320 (1993) 71-74.

32. M.L. Genova, G. Lenaz, A critical appraisal of the role of respiratory supercomplexes in mitochondria, *Biol. Chem*. 394 (2013) 631-639.

33. J. Stonehuerner, P. O'Brien, L. Geren, F. Millett, J. Steidl, L. Yu, C. Yu, Identification of the binding site on cytochrome c_1 for cytochrome *c*, *J. Biol. Chem*. 260 (1985) 5392-5398.

34. P.B. Crowley, K.S. Rabe, J.A. Worrall, G.W. Canters, M. Ubbink, The ternary complex of cytochrome *f* and cytochrome *c*: identification of a second binding site and competition for plastocyanin binding, *Chembiochem* 3 (2002) 526-533.

35. I. Díaz-Moreno, A. Díaz-Quintana, M.A. De la Rosa, P.B. Crowley, M. Ubbink, Different modes of interaction in cyanobacterial complexes of plastocyanin and cytochrome *f*, *Biochemistry* 44 (2005a) 3176-3183.

36. B.S. Rajagopal, A.N. Edzuma, M.A. Hough, K.L. Blundell, V.E. Kagan, A.A. Kapralov, L.A. Fraser, J.N. Butt, G.G. Silkstone, M.T. Wilson, D.A. Svistunenko, J.A. Worrall, The hydrogen-peroxide-induced radical behaviour in human cytochrome c-phospholipid complexes: implications for the enhanced pro-apoptotic activity of the G41S mutant, *Biochem. J*. 456 (2013) 441-452.

37. W. Rocchia, S. Sridharan, A. Nicholls, E. Alexov, A. Chiabrera, B. Honig, Rapid grid-based construction of the molecular surface and the use of induced surface charge to calculate reaction field energies: applications to the molecular systems and geometric objects, *J. Comput. Chem.* 23 (2002) 128-137.

38. E.F. Pettersen, T.D. Goddard, C.C. Huang, G.S. Couch, D.M. Greenblatt, E.C. Meng, T.E. Ferrin, UCSF Chimera- A visualization system for exploratory research and analysis, *J. Comput. Chem*. 25 (2004) 1605-1612.

39. A. Olteanu, C.N. Patel, M.M. Dedmon, S. Kennedy, M.W. Linhoff, C.M. Minder, P.R. Potts, M. Deshmukh, G.J. Pielak, Stability and apoptotic activity of recombinant human cytochrome *c*, *Biochem. Biophys. Res. Commun*. 312 (2003) 733-740.

40. A. Díaz, F. Navarro, M. Hervás, J.A. Navarro, S. Chávez, F.J. Florencio, M.A. De la Rosa, Cloning and correct expression in *E. coli* of the petJ gene encoding cytochrome c_6 from *Synechocystis* 6803, *FEBS Lett*. 347 (1994) 173-177.
41. J.A. Navarro, M. Hervás, B. De la Cerda, M.A. De la Rosa, Purification and physicochemical properties of the low-potential cytochrome c_{549} from the cyanobacterium *Synechocystis* sp. PCC 6803, *Arch. Biochem. Biophys.* 318 (1995) 46-52.
42. F.P. Molina-Heredia, M. Hervás, J.A. Navarro, M.A. De la Rosa, Cloning and correct expression in *Escherichia coli* of the petE and petJ genes respectively encoding plastocyanin and cytochrome c_6 from the cyanobacterium *Anabaena* sp. PCC 7119, *Biochem. Biophys. Res. Commun*. 243 (1998) 302-306.
43. C. Frazao, F.J. Enguita, R. Coelho, G.M. Sheldrick, J.A. Navarro, M. Hervás, M.A. De la Rosa, M.A. Carrondo, Crystal structure of low-potential cytochrome c_{549} from *Synechocystis* sp. PCC 6803 at 1.21 A resolution, *J. Biol. Inorg. Chem.* 6 (2001) 324-332.
44. W. Jeng, C. Chen, H. Chang, W. Chuang, Expression and Characterization of Recombinant Human Cytochrome *c* in *E. coli*, *J. Bioenerg. Biomembr*. 34 (2002) 423-431.
45. E. Freire, A. Schön, A. Velázquez-Campoy, Isothermal titration calorimetry: general formalism using binding polynomials, *Methods Enzymol*. 455 (2009), 127-155.
46. F.P. Molina-Heredia, A. Díaz-Quintana, M. Hervás, J.A. Navarro, M.A. De la Rosa, Site-directed mutagenesis of cytochrome c_6 from *Anabaena* species PCC 7119. Identification of surface residues of the hemeprotein involved in photosystem I reduction, *J. Biol. Chem*. 274 (1999) 33565-33570.
47. P.B. Crowley, A. Díaz-Quintana, F.P. Molina-Heredia, P. Nieto, M. Sutter, W. Haehnel, M.A. De la Rosa, M. Ubbink, The interactions of cyanobacterial

cytochrome c_6 and cytochrome *f*, characterized by NMR, *J. Biol. Chem*. 277 (2002) 48685-48689.

48. I. Díaz-Moreno, A. Díaz-Quintana, M.A. De la Rosa, M. Ubbink, Structure of the complex between plastocyanin and cytochrome *f* from the cyanobacterium *Nostoc sp. PCC 7119* as determined by paramagnetic NMR. The balance between electrostatic and hydrophobic interactions within the transient complex determines the relative orientation of the two proteins, *J. Biol. Chem*. 280 (2005b) 18908-18915.
49. I. Díaz-Moreno, A. Díaz-Quintana, F.P. Molina-Heredia, P.M. Nieto, O. Hansson, M.A. De la Rosa, B.G. Karlsson, NMR analysis of the transient complex between membrane photosystem I and soluble cytochrome c_6, *J. Biol. Chem*. 280 (2005c) 7925-7931.
50. I. Díaz-Moreno, A. Díaz-Quintana, M. Ubbink, M.A. De la Rosa, An NMR-based docking model for the physiological transient complex between cytochrome *f* and cytochrome c_6, *FEBS Lett*. 579 (2005d) 2891-2896.
51. A.N. Volkov, J.A. Worrall, E. Holtzmann, M. Ubbink, Solution structure and dynamics of the complex between cytochrome *c* and cytochrome *c* peroxidase determined by paramagnetic NMR, *Proc. Natl. Acad. Sci.* USA 103 (2006) 18945-18950.
52. K. Sakamoto, M. Kamiya, M. Imai, K. Shinzawa-Itoh, T. Uchida, K. Kawano, S. Yoshikawa, K. Ishimori, NMR basis for interprotein electron transfer gating between cytochrome *c* and cytochrome *c* oxidase, *Proc. Natl. Acad. Sci.* USA 108 (2011) 12271-12276.
53. M. Hervás, Q. Bashir, N.G. Leferink, P. Ferreira, B. Moreno-Beltrán, A.H. Westphal, I. Díaz-Moreno, M. Medina, M.A. De la Rosa, M. Ubbink, J.A. Navarro, W.J. van Berkel, Communication between (L)-galactono-1,4-lactone dehydrogenase and cytochrome *c*, *FEBS J.* 280 (2013) 1830-1840.

54. I. Díaz-Moreno, R. Hulsker, P. Skubak, J.M. Foerster, D. Cavazzini, M.G. Finiguerra, A. Díaz-Quintana, B. Moreno-Beltrán, G.L. Rossi, G.M. Ullmann, N.S. Pannu, M.A. De la Rosa, M. Ubbink, The dynamic complex of cytochrome c_6 and cytochrome *f* studied with paramagnetic NMR spectroscopy, *Biochim. Biophys. Acta* 1837 (2014) 1305-1315.
55. M. De March, N. Demitri, R. De Zorzi, A. Casini, C. Gabbiani, A. Guerri, L. Messori, S. Geremia, Nitrate as a probe of cytochrome *c* surface: Crystallographic identification of crucial “hot spots” for protein-protein recognition, *J. Inorg. Bioch.* 135 (2014) 58-67.
56. S.H. Speck, S. Ferguson-Miller, N. Osheroff, E. Margoliash, Definition of cytochrome *c* binding domains by chemical modification: kinetics of reaction with beef mitochondrial reductase and functional organization of the respiratory chain, *Proc. Natl. Acad. Sci.* USA 76 (1979) 155-159.
57. B.W. König, N. Osheroff, J. Wilms, A.O. Muijsers, H.L. Dekker, E. Margoliash, Mapping of the interaction domain for purified cytochrome c_1 on cytochrome *c*, *FEBS Lett*. 111 (1980) 395-398.
58. O. Kokhan, C.A. Wraight, E. Tajkhorshid, The binding interface of cytochrome *c* and cytochrome c_1 in the bc_1 complex: rationalizing the role of key residues, *Biophys. J*. 99 (2010) 2647-2656.
59. T.R. Schmidt, D.E. Wildman, M. Uddin, J.C. Opazo, M. Goodman, L.I. Grossman, Rapid electrostatic evolution at the binding site for cytochrome *c* on cytochrome *c* oxidase in anthropoid primates, *Proc. Natl. Acad. Sci.* USA 102 (2005) 6379-6384.
60. D. Pierron, D.E. Wildman, M. Hüttemann, T. Letellier, L.I. Grossman, Evolution of the couple cytochrome *c* and cytochrome *c* oxidase in primates, *Adv. Exp. Med. Biol.* 748 (2012) 185-213.

61. M. Medina, M. Hervás, J.A. Navarro, M.A. De la Rosa, C. Gómez-Moreno, G. Tollin, A laser flash absorption spectroscopy study of *Anabaena* sp. PCC 7119 flavodoxin photoreduction by photosystem I particles from spinach, *FEBS Lett*. 313 (1992) 239-242.

62. A. Díaz, M. Hervás, J.A. Navarro, M.A. De la Rosa, G. Tollin, A thermodynamic study by laser-flash photolysis of plastocyanin and cytochrome c_6 oxidation by photosystem I from the green alga *Monoraphidium braunii*, *Eur. J. Biochem*. 222 (1994) 1001-1007.

63. J. Sun, W. Xu, M. Hervás, J.A. Navarro, M.A. Rosa, P.R. Chitnis, Oxidizing side of the cyanobacteria photosystem I. Evidence for interaction between the electron donor proteins and a luminal surface helix of the PsaB subunit, *J. Biol. Chem.* 274 (1999) 19048-19054.

64. J.L. Casaus, J.A. Navarro, M. Hervás, A. Lostao, M.A. De la Rosa, C. Gómez-Moreno, J. Sancho, M. Medina, *Anabaena* sp. PCC 7119 flavodoxin as electron carrier from photosystem I to ferredoxin-NADP+ reductase. Role of Trp(57) and Tyr(94), *J. Biol. Chem.* 277 (2002) 22338-22344.

65. S. Scanu, J.M. Foerster, G.M. Ullmann, M. Ubbink, Role of hydrophobic interactions in the encounter complex formation of the plastocyanin and cytochrome *f* complex revealed by paramagnetic NMR spectroscopy, *J. Am. Chem. Soc.* 135 (2013) 7681-7692.

66. N. Osheroff, S.H. Speck, E. Margoliash, E.C. Veerman, J. Wilms, B.W. König, A.O. Muijsers, The reaction of primate cytochromes *c* with cytochrome *c* oxidase. Analysis of the polarographic assay, *J. Biol. Chem.* 258 (1983) 5731-5738.

67. J.A. Navarro, R.V. Durán, M.A. De la Rosa, M. Hervás, Respiratory cytochrome *c* oxidase can be efficiently reduced by the photosynthetic redox proteins

cytochrome c_6 and plastocyanin in cyanobacteria, *FEBS Lett.* 579 (2005) 3565-3568.

68. E. Lapuente-Brun, R. Moreno-Loshuertos, R. Acín-Pérez, A. Latorre-Pellicer, C. Colás, E. Balsa, E. Perales-Clemente, P.M. Quirós, E. Calvo, M.A. Rodríguez-Hernández, P. Navas, R. Cruz, Á. Carracedo, C. López-Otín, A. Pérez-Martos, P. Fernández-Silva, E. Fernández-Vizarra, J.A. Enríquez, Supercomplex assembly determines electron flux in the mitochondrial electron transport chain, *Science* 340 (2013) 1567-1570.

Table 1. Equilibrium and thermodynamic parameters for the interaction of hC*c* at the two sites of pCc_1.

Equilibrium dissociation constants (K_{D1} and K_{D2}), enthalpies (ΔH_1 and ΔH_2), entropies ($-T\Delta S_1$ and $-T\Delta S_2$), Gibbs free energies (ΔG_1 and ΔG_2) and stoichiometry of the reaction (n) were determined by CSP or ITC for the reduced (hCc_{red}–pCc_{1red}) and oxidized (hCc_{ox}–pCc_{1ox}) complexes. Parameters for the hCc_{red}-pCc_{1red} interaction in the presence of 50 or 100 mM NaCl are also shown.

Protein couple	***Proximal* site**				***Distal* site**				
	K_{D1} (μM)	ΔH_1 (kcal mol^{-1})	$-T\Delta S_1$ (kcal mol^{-1})	ΔG_1 (kcal mol^{-1})	K_{D2} (μM)	ΔH_2 (kcal mol^{-1})	$-T\Delta S_2$ (kcal mol^{-1})	ΔG_2 (kcal mol^{-1})	n
hCc_{red}-pCc_{1red}[a]	0.3	n.d.	n.d.	-8.9	40.0	n.d.	n.d.	-6.0	2
hCc_{red}-pCc_{1red}[b]	11.5	11.7	-18.4	-6.7	54.0	10.5	-16.3	-5.8	2
hCc_{ox}-pCc_{1ox}[b]	9.4	6.2	-13.0	-6.8	86.0	14.6	-20.1	-5.5	2
hCc_{red}-pCc_{1red}[a*]	12.8	n.d.	n.d.	-6.6					1
hCc_{red}-pCc_{1red}[b*]	69	7.8	-13.4	-5.6					1
hCc_{red}-pCc_{1red}[b**]	230	17.4	-22.3	-4.9					1

n.d., not determined.
[a] CSP.
[b] ITC.
[*] 50 mM NaCl added.
[**] 100 mM NaCl added.
Relative errors: K_D 20%, ΔH and $-T\Delta S$ 5%, ΔG 2%.

Figure 1

Figure 1

Click here to download Figure: MorenoBeltran_et al - FEBS Lett - Figure 1.pdf

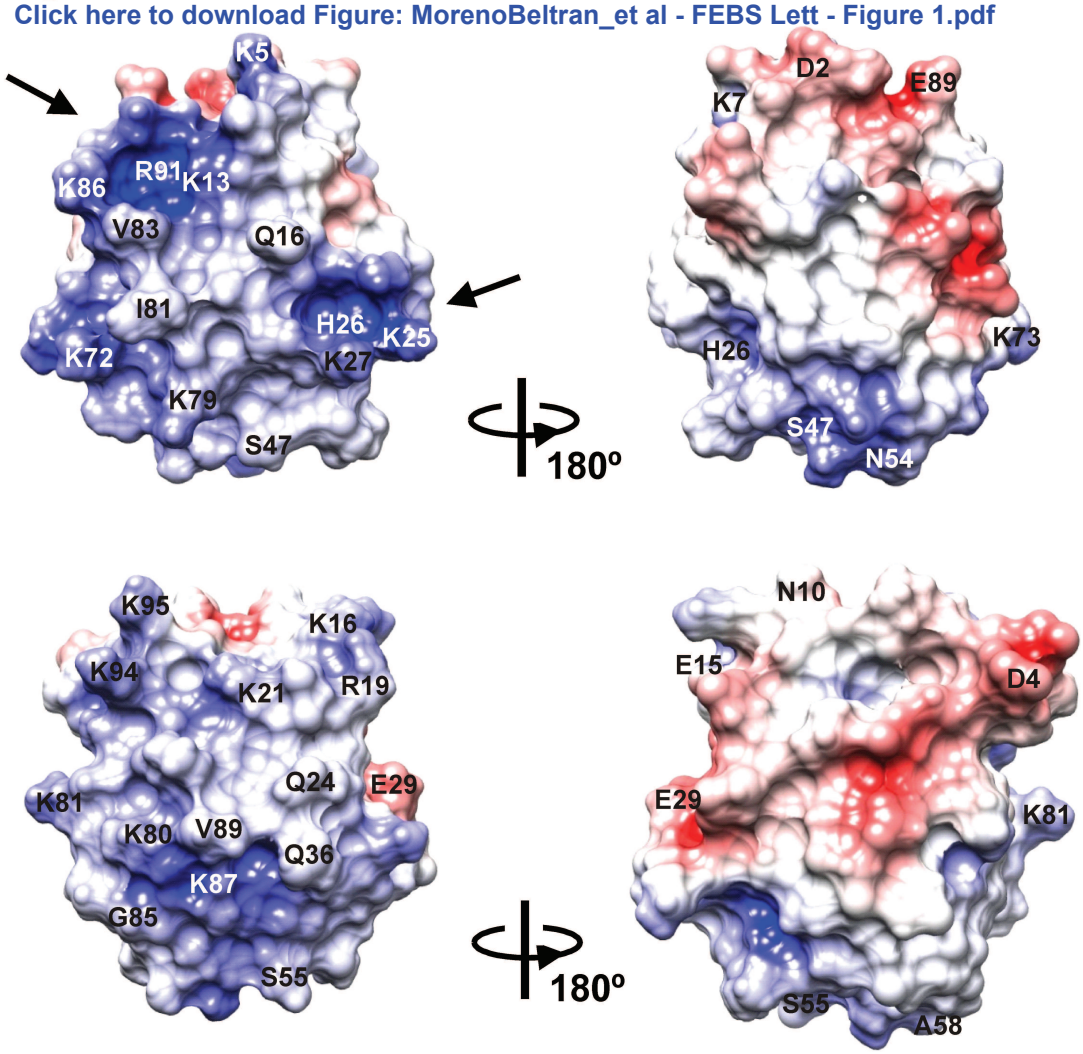

Figure 2

Click here to download Figure: MorenoBeltran_et al - FEBS Lett - Figure 2.pdf

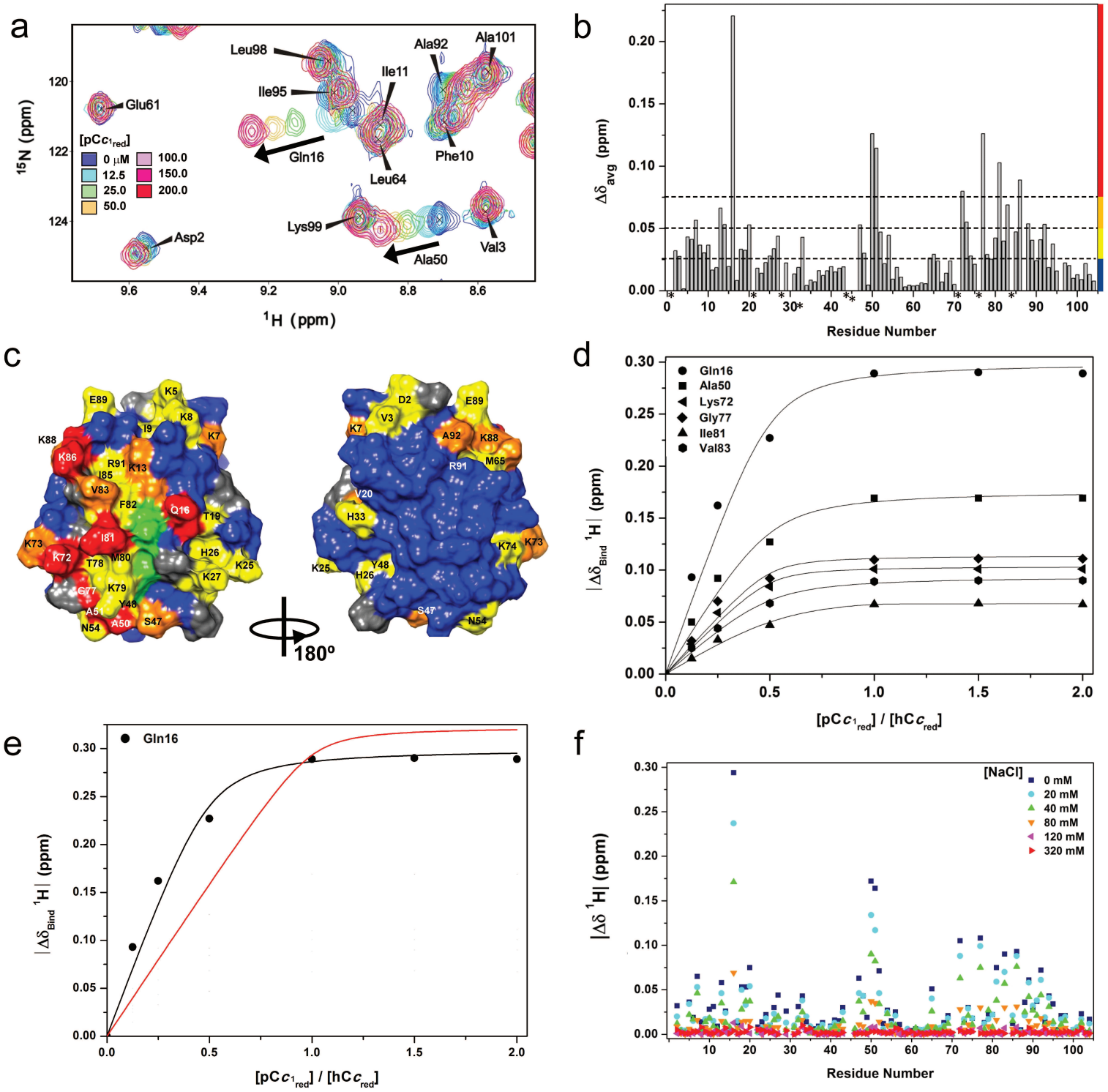

Figure 3

Click here to download high resolution image

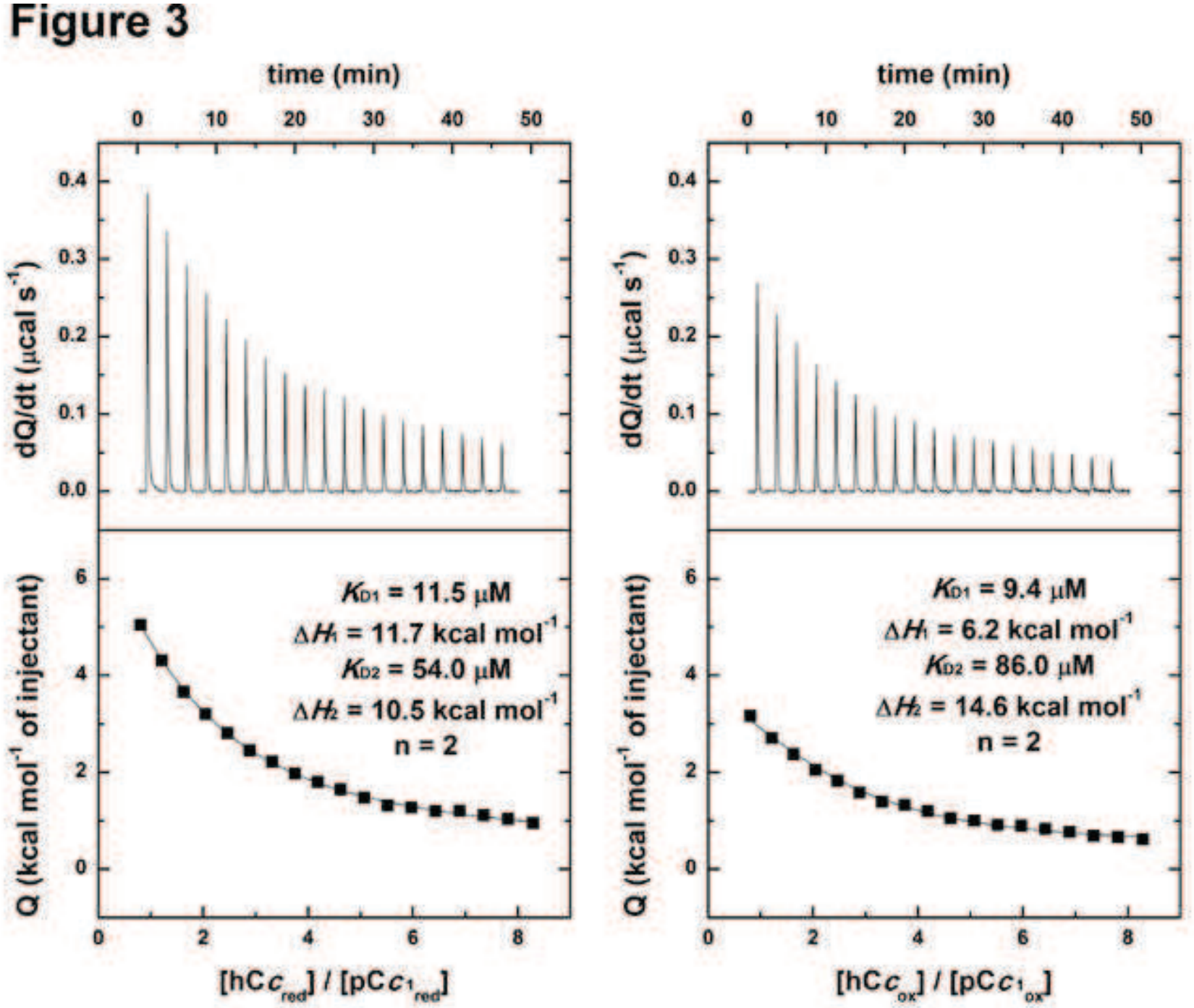

Figure 4

Figure 4

Click here to download Figure: MorenoBeltran_et al - FEBS Let

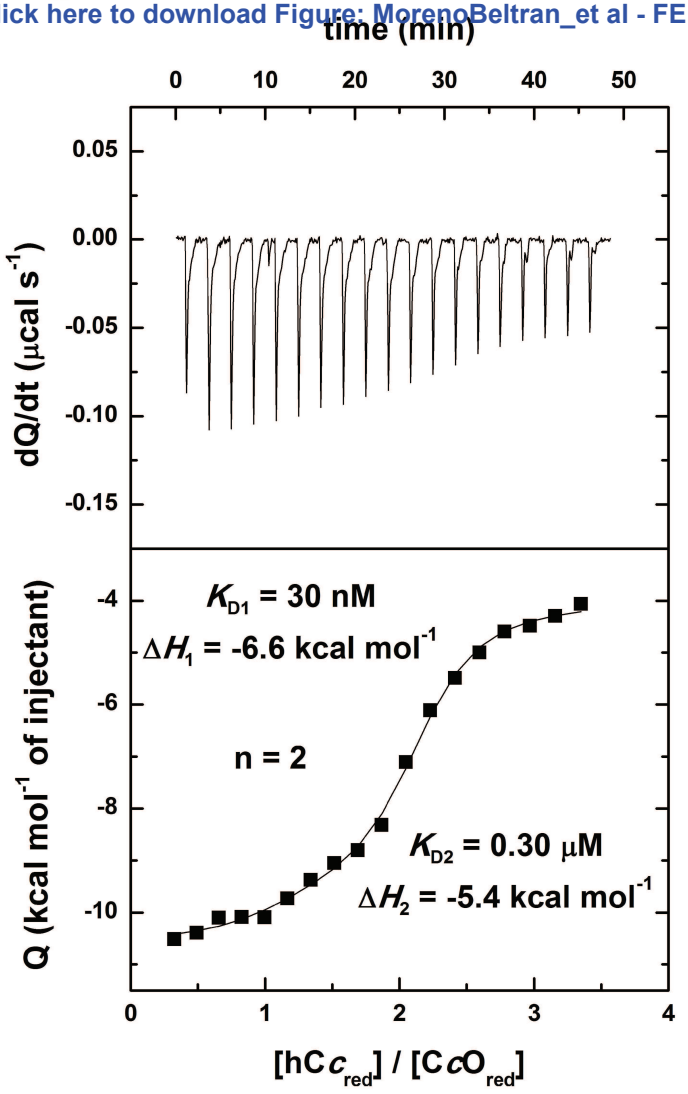

Figure 5
Click here to download high resolution image